

Dependable contact related parameter extraction in graphene - metal junctions

Amit Gahoi^a, Satender Kataria^a, Francesco Driussi^b, Stefano Venica^b, Himadri Pandey^a, David Esseni^b,

Luca Selmi^c, M. C. Lemme^{a, d*}

^aRWTH Aachen University, Faculty of Electrical Engineering and Information Technology, Chair of Electronic Devices, Otto-Blumenthal-Str. 2, 52074 Aachen, Germany

^bUniversità degli Studi di Udine, Dipartimento Politecnico di Ingegneria e Architettura (DPIA), Via delle Scienze 206, 33100 Udine, Italy

^cUniversità degli Studi di Modena e Reggio Emilia, Dipartimento di Ingegneria "Enzo Ferrari", Via Vivarelli 10, 41125 Modena, Italy

^dAMO GmbH, Advanced Microelectronic Center Aachen (AMICA), Otto-Blumenthal-Str. 25, 52074 Aachen, Germany

*Corresponding author: max.lemme@eld.rwth-aachen.de, lemme@amo.de

Abstract – The accurate extraction and the reliable, repeatable reduction of graphene – metal contact resistance (R_C) are still open issues in graphene technology. Here, we demonstrate the importance of following clear protocols when extracting R_C using the transfer length method (TLM). We use the example of back-gated graphene TLM structures with nickel contacts, a complementary metal oxide semiconductor compatible metal. The accurate extraction of R_C is significantly affected by generally observable Dirac voltage shifts with increasing channel lengths in ambient conditions. R_C is generally a function of the carrier density in graphene. Hence, the position of the Fermi level and the gate voltage impact the extraction of R_C . Measurements in high

vacuum, on the other hand, result in dependable extraction of R_C as a function of gate voltage owing to minimal spread in Dirac voltages. We further assess the accurate measurement and extraction of important parameters like contact-end resistance, transfer length, sheet resistance of graphene under the metal contact and specific contact resistivity as a function of the back-gate voltage. The presented methodology has also been applied to devices with gold and copper contacts, with similar conclusions.

Keywords: CVD graphene, graphene – metal contact, transfer length method, contact resistance, transmission line model, specific contact resistivity, sheet resistance.

1. INTRODUCTION

Graphene exhibits unique and remarkable physical, chemical and electrical properties [1]. It is considered as a promising material for electronic devices and applications. The extraordinary features of graphene have been explored in numerous device demonstrations such as radio frequency (RF) analog transistors [2]–[7], photodetectors [8]–[12], nanoelectromechanical systems [13]–[17] or terahertz modulators [18]–[20]. Low resistivity electrical contacts are fundamental for all of these applications as they provide means for communication between the active devices and the outside world [21]. Because of the low density of states in graphene [22], the charge injection into graphene leads to a high contact resistance (R_C) at graphene – metal (G-M) junctions [23], that may be a serious limiting factor for graphene devices. To achieve low contact resistivity, nanostructuring or engineering of graphene under the contact metals have displayed some potential [24]–[26]. Nevertheless, reported values of R_C found in literature vary considerably [27]–[30], which can be attributed to intrinsic factors such as the quality of graphene layers, work functions of the metals (ϕ_M) or doping of graphene and to extrinsic factors such as specific fabrication procedures. However, there is also a debate on the applicability of standard

measurement and extraction methods to obtain dependable and correct R_C values. In particular, the transfer length method (TLM) is widely used to extract R_C from test structures. It has been suggested and demonstrated that the classic TLM may be inappropriate under certain conditions for characterizing G-M contacts [31]–[35]. Since the sheet resistance of the graphene channel (R_{SH}) is a dominating component of the total resistance of the device (R_T) and since the TLM technique is based on the comparison of the R_T values of the GFETs inside the TLM structure, slight changes in R_{SH} along the TLM array will lead to erroneous R_C values. In addition, the R_{SH} is different from the sheet resistance of graphene under the metal contact (R_{SK}) due to the G-M interactions that dope graphene [27], [36], [37] and this should be accounted for in the extraction of the parameters describing the G-M junction.

Here, we present a comprehensive analysis of the TLM technique for extracting R_C in two-dimensional (2D) graphene devices using nickel (Ni) as contact metal. The analysis is further implemented and verified using copper (Cu) and gold (Au) contacts as well for generalization. In the following, we use an extended terminology, where the extracted R_C is called contact front resistance (R_{CF}). R_{CF} is extracted from a measured voltage drop at the source/drain contacts that depends on the contact shape and size (i.e. geometry dependent), the charge carrier density (n_0) in graphene under the metal contact and the specific contact resistivity ρ_c , which is geometrically independent. These additional parameters can be obtained by measuring the contact end resistance (R_{CE}) [38], which allows extracting ρ_c , the R_{SK} and the transfer length (L_{TK}). Furthermore, R_{SK} can be compared to R_{SH} to gain insight into the impact of the contact metal proximity to the graphene on the graphene charge. Finally, the developed method enables the identification of extrinsic effects which significantly affect the extraction of R_{CF} by comparing measurements performed in

ambient and vacuum conditions ($\sim 10^{-6}$ mbar). In particular, the shift of the Dirac voltage (V_{DIRAC}) in devices with different channel length (L_{CH}) influences the variability of the extracted data.

2. THEORY

In the TLM measurement technique, R_{CF} is extracted from the total measured resistance (R_{T}) of the device, which comprises of the sheet resistance of graphene channel (R_{SH}), two times R_{CF} and the parasitic resistances (which are generally neglected) of the metal contact pad, probe needles and leads. Here, R_{T} of a GFET is extracted by applying a voltage V_{12} between contacts 1 and 2 and measuring the current I_{12} as shown in Fig. 1 (a). Therefore,

$$R_{\text{T}} = \frac{V_{12}}{I_{12}} \quad (1)$$

As mentioned above, the R_{T} of the device can be deconvoluted into

$$R_{\text{T}} = 2R_{\text{CF}} + \frac{R_{\text{SH}} * L_{\text{CH}}}{W_{\text{CH}}} + 2R_{\text{M}} \quad (2)$$

where R_{M} is the resistance of the metal that is generally neglected ($R_{\text{M}} \ll R_{\text{SH}}$). R_{CF} and R_{SH} are extracted by the TLM extrapolation technique. More details about the TLM extraction technique are reported in the supplementary information (section B). Fig. 1(b) explicitly explains about various resistive components at G-M junction. In Fig. 1(b), for the contact 2, $X = 0$ corresponds to the front edge of the contact, while $X = d$ is at the end of the contact (where $d = 4 \mu\text{m}$ is the length of the fabricated contact). R_{CF} is defined as the ratio of the voltage drop across the interfacial layer at the front edge of the contact, where the current density is greatest ($X=0$) as shown in Fig. 1 (b). R_{CE} instead is defined through the voltage drop across the interfacial layer at the edge of the contact, where the current density is least ($X=d$) as depicted in Fig. 1 (b).

As metal can dope graphene at the contact regions [39], R_{SK} may be different from the R_{SH} [27]. If $R_{SK} \neq R_{SH}$, the extraction of L_{TK} , described in detail in the supplementary information (section C), by using the conventional extraction through the TLM method leads to erroneous L_{TK} values. In such a situation, additional measurements are required to extract reliable contact related parameters at the G-M junction, namely the R_{CE} technique [33], [38]. R_{CE} can be measured directly by forcing a known current between contacts 1 and 2 and measuring the generated voltage drop across the G-M stack, while imposing a null current on contact 3 as shown in Fig. 1 (a). In this way, R_{CE} is measured by the use of the additional contact 3, since by forcing a null current, there is no additional voltage drop between contacts 2 and 3. So we have:

$$R_{CE} = \frac{V_{32}}{I_{12}} \quad (3)$$

The R_{CE} measurement does not depend on the graphene quality outside the metal, which removes errors caused by inhomogeneities of the graphene channel.

Figure 1 (c) is the distributed resistance network describing the transmission line model typically used to describe the G-M contacts. Here, the current is highest at front edge of the contact ($X=0$) and drops exponentially with the distance (represented by a yellow line as $J_v(x)$). The “ $1/e$ ” distance of the voltage drop profile from the front edge of the contact is defined as L_{TK} . In layman terms, L_{TK} is the effective electrical length of the contact. The transmission line model equations [38] can be used to extract ρ_c , R_{SK} and L_{TK} by using the R_{CF} and R_{CE} values measured with the procedure explained above. Further details on this point are provided in section C of the supporting information.

3. RESULTS AND DISCUSSION

Large - area monolayer graphene was grown on a copper (Cu) foil via chemical vapor deposition (CVD) process in a NanoCVD (Moorfield, UK) rapid thermal processing tool [40]. Silicon wafers (p-doped) with resistivity ($1\text{-}20\ \Omega\mu\text{m}$) were used as a starting substrate and thermally oxidized to achieve a thickness of 85 nm. CVD graphene was transferred onto the silicon/silicon dioxide (Si/SiO₂) substrate using an electrochemical delamination technique [41]. Photolithography and reactive ion etching (RIE) were used to define graphene channels using an oxygen plasma process. Nickel (Ni), Copper (Cu) and gold (Au) metals were thermally evaporated to contact graphene, and a lift-off process was carried out in order to define source-drain contact pads. Subsequently, rapid thermal annealing (RTA) process was carried out for 2 hours in an argon (95%)/hydrogen (5%) atmosphere at 450°C to minimize the PMMA residue and to enhance the G-M contact bonding [42]. Figure 2(a) shows a scanning electron micrograph (SEM) of a complete TLM structure with a channel width of $W_{\text{CH}} = 20\ \mu\text{m}$ and L_{CH} ranging from $5\ \mu\text{m}$ till $50\ \mu\text{m}$. Figure 2 (b) shows a Raman area map of the 2D band intensity in one of the TLM channels, indicated by the blue square in the optical micrograph. A mostly uniform intensity distribution was observed which pointed towards homogenous graphene layers. Figure 2 (c) shows the Raman spectrum of the graphene taken before and after the final device fabrication on SiO₂/Si substrate. The red curve is the Raman spectrum of graphene just after the transfer with a ratio of $I_{2\text{D}}/I_{\text{G}}$ close to 2, confirming the high quality of the monolayer graphene. The potential presence of some graphene adlayers and grain boundaries result in a small D peak. The TLM structures were vacuum annealed after final device fabrication to enhance the G-M bonding [42]. The black curve in Fig. 2 (c) shows the Raman spectrum of graphene after the annealing process. The 2D/G peak intensity ratio was less than 1 with sharper 2D and G peaks. Such features in Raman spectra of annealed graphene samples point

towards strong p-doping of substrate-supported graphene in ambient conditions after the annealing process [43]–[45]. It is worth noticing that the concept of “doping” is here used to describe a change in the Fermi level / carrier density in the graphene due to mirror charges and not the replacement of graphene atoms by dopants as in conventional semiconductor technology. A broad peak observed near the D peak can be attributed to amorphous carbon byproducts formed by carbonization of residual polymer layers on graphene surface [45].

Electrical characterization was carried out in a Lakeshore probe station with a Keithley SCS4200 parameter analyzer in ambient air and in vacuum ($\sim 10^{-6}$ mbar). The samples were kept in Lakeshore for a period of 48 hours to achieve optimum vacuum before measurement. Electrical characterization in ambient atmosphere is carried out by keeping chamber open (humidity $\sim 21\%$, temperature ~ 300 K). Figure 3 (a) shows the transfer characteristics [source-drain current (I_{DS}) vs back-gate voltage (V_{BG})] of Ni contacted graphene (G – Ni) measured in ambient air. The Dirac voltages (V_{DIRAC}) are located at positive V_{BG} , indicating a p-doping of the graphene channel [31], [32], [46]. This is in agreement with Raman measurements [Fig. 2(c)], where signatures of p-doping of graphene were observed. This observation can be ascribed to adsorbed water molecules on top of the graphene surface [15]. Graphene acts as an electron donor when water molecules come in contact, leading to the shift of the V_{DIRAC} towards positive gate-voltages, with a charge transfer to graphene per water molecule of approximately $0.002e$ [47]. We noted a further V_{DIRAC} shift towards positive V_{BG} when L_{CH} increases as summarized in Fig. 3(d). A similar V_{DIRAC} shift was observed by Han et al. in a mechanically exfoliated graphene device and they attributed it to the short channel effects in graphene [48]. However, in our case, short channel effects do not apply. Instead, the effect may be attributed to the polycrystalline nature of the CVD monolayer graphene. Grain boundaries in CVD graphene have been shown to act as active sites for adsorbates like water

molecules [49], which can be revealed using HF vapor etching [50]. In the present case, the number of grain boundaries in a device channel should increase with increasing L_{CH} , because the device dimensions of the smallest devices are of the same order of magnitude as the grains. Hence, an increased number of grain boundaries in larger devices increases the effect of water adsorbates with L_{CH} . Figure 3 (b) is the schematic representation of a TLM structure with varied L_{CH} showing grain boundaries in the CVD graphene.

In vacuum, V_{DIRAC} is significantly shifted compared to ambient air and is observed near -5V, i.e. the graphene channel is slightly n-doped [Fig. 3(c)]. Similar behavior has been observed in Di Bartolomeo et al. [51]. This indicates successful removal of adsorbates by vacuum. This is confirmed by cycling the devices from ambient conditions to vacuum, which shifts V_{DIRAC} consistently back and forth between negative and positive voltages (see section A in the supplementary information). We further found that the V_{DIRAC} difference between different L_{CH} was negligible under vacuum conditions as reported in Fig. 3(d). This supports our assumption concerning the significant role played by grain boundaries and other defects as adsorption sites in ambient condition. These results clearly show that vacuum measurements are required for reliable extraction of R_{CF} . Alternatively, controlled encapsulation with dielectrics may be feasible [52], although this is still a field of further research [21].

Having established the large impact of the environment conditions on the device characteristics (I_{DS} vs. V_{BG}), we now concentrate on the dependable extraction of the parameters related to G – M contacts. The extraction of R_{CF} for G - Ni contacts [Fig. 3 (a)] when the measurement (I_{DS} – V_{BG}) were carried out in ambient air results in erroneous values for varying V_{BG} . For example, R_{CF} values of $100 \pm 311 \Omega\mu m$ at $V_{BG} = -20$ V [Fig. 4(a)] and of $-2585 \pm 1560 \Omega\mu m$ at $V_{BG} = 20$ V [Fig. 4(b)] are extracted, despite achieving high quality fitting ($0.97 < R^2 < 0.999$) of the R_T vs L_{CH}

curve. Since negative R_{CF} values are not possible in any junction, the source for these errors must be in the extraction technique. In contrast, the TLM measurements under vacuum led to reasonable values of R_{CF} ; in particular $876 \pm 367 \Omega\mu\text{m}$ is extracted at $V_{BG} = -20 \text{ V}$ [Fig. 4(c)] and $1140 \pm 234 \Omega\mu\text{m}$ is extracted at $V_{BG} = 20 \text{ V}$ [Fig. 4(d)], respectively. This large difference between data in ambient air and high vacuum is also due to the large distortion induced by the air to the $I_{DS} - V_{BG}$ curves in Fig. 4(e) ($L_{CH} = 5 \mu\text{m}$ and $W_{CH} = 20 \mu\text{m}$). In particular, there is a decrease in the conductivity when the devices are measured in high vacuum, which can be attributed to the removal of water adsorbents from the graphene surface, that provide p-doping to graphene and thus a higher charge density n_0 and a higher conductivity. Figure 4 (f) shows the V_{BG} dependence of R_{CF} for the TLM devices measured in high vacuum. R_{CF} clearly is V_{BG} dependent, with a peak at V_{DIRAC} , while it decreases as the graphene channel is electrostatically doped by V_{BG} . However, despite measuring the devices in vacuum, the extraction of R_{CF} leads to an unusually and, more important, unphysically low value at $V_{BG} = -10 \text{ V}$. Current measurements in high vacuum demonstrate a minimum conductance around $V_{BG} \sim -5 \text{ V}$, with this value varying by less than 0.5 V across the TLM array. To avoid this effect of marginal V_{DIRAC} shifts with varied L_{CH} , the minimum conductivity points of all the channels was normalized to 0 V to ensure the same n_0 in the graphene channels when comparing the R_T values as discussed in [53]. This normalization process was also applied to the measurements done in air, but the obtained results were unphysical (see section D of the supplementary information).

Figure 5 (a) shows the normalized transfer characteristics [I_{DS} vs. $(V_{BG} - V_{DIRAC})$] for different L_{CH} of the G - Ni samples measured in vacuum. Figure 5 (b) shows the R_{CF} values extracted through the TLM method after the normalization. The R_{CF} values peak at $(V_{BG} - V_{DIRAC})=0$, so at the minimum conduction point for graphene. This suggests that the conventional TLM extrapolation

technique for R_{CF} is valid only when maintaining the same n_0 in graphene channels with different L_{CH} . A slight difference in the n_0 among the channels leads to large errors in the R_{CF} values [see Figs. 4 (a) and (b)] [48].

Figure 5 (c) shows R_{CE} as a function of L_{CH} at different V_{BG} extracted by using the measurement setup shown in Fig. 1 (a). R_{CE} ranges from 10.5Ω to 12Ω with respect to L_{CH} at a fixed V_{BG} demonstrating that R_{CE} is more or less unaffected by the channel resistance outside the contact [33], [54]. The R_{CE} measurement was also carried out in ambient air at $V_{BG} = 0V$ [Fig. 5 (d)] and found to be very consistent with the results in vacuum, which indicates that R_{CE} is unaffected by the channel conductivity and, thus, by the measurements conditions (in this case graphene is protected from water molecules by the contact on the top). Finally, R_{CE} is rather independent of V_{BG} and this is most likely because its value is linked to the voltage drop at the end of the contact, where the current density is null and so the V_{BG} dependence this latter is not effective.

R_{CE} and R_{CF} values were then used to calculate ρ_c , L_{TK} and R_{SK} (see section C of the supplementary information). Figure 5 (e) shows L_{TK} extracted from measurements done in vacuum as a function of $(V_{BG} - V_{DIRAC})$. L_{TK} is around $1.4 \mu m$ at $n_0 = 8.69 \times 10^{12} cm^{-2}$ and decreases to $0.9 \mu m$ at $n_0 = 1.01 \times 10^{12} cm^{-2}$. Figure 5 (f) instead reports the ρ_c as a function of $(V_{BG} - V_{DIRAC})$ and ρ_c is $2.44 \times 10^{-5} \Omega cm^2$ at $n_0 = 8.69 \times 10^{12} cm^{-2}$ and $7.38 \times 10^{-5} \Omega cm^2$ at $n_0 = 1.01 \times 10^{12} cm^{-2}$. Error bars indicate upper limits and lower limits in fitting the measured data and they are quite large near V_{DIRAC} . Finally, R_{SH} and R_{SK} were extracted to determine the impact of the metal on the properties of graphene under the contact. Figure 5 (g) shows R_{SK} and R_{SH} extracted as a function of V_{BG} . R_{SK} for Ni contacts is larger than the R_{SH} . Although it has been shown that the p-orbitals of graphene hybridize strongly with Ni d-states [55], the extracted ρ_c and R_{SK} are quite high. This can likely be attributed to nickel-carbide formation at the interface, which can be detrimental for the charge

carriers transport through the G-M junction [55]. This is even more important at the Dirac point, where R_{SK} shows a large peak. This is most likely due to the fact that hybridization of graphene orbitals induces small band-gaps at the K-point in the graphene bands [56]. This reduces the graphene charge at the Dirac point, largely impacting the R_{SK} value.

As discussed above, R_{CF} is intrinsically dependent on the charge density in graphene and in the metal. In the case of metal, it is extremely high and in the order of $\sim 10^{21} \text{ cm}^{-3}$, so it does not limit the current and its effect can be neglected. In the case of graphene, n_0 typically varies between 10^{11} and 10^{13} cm^{-2} , therefore R_{CF} is intrinsically dependent on the R_{SK} of graphene under the metal contact [57]. Therefore, it is important to fabricate high quality graphene to lower R_{SK} and thus to reduce R_{CF} [58]. Also selecting the metal materials that increase n_0 in the underneath graphene would improve R_{SK} and hence R_{CF} .

The methodology described for G-Ni contacts was also applied to the case of graphene – copper (G – Cu) and graphene – gold (G – Au) contacts (see section E in the supplementary information). Furthermore, extensive measurements and extractions were also carried out for TLM devices with G – Au contacts measured in ambient air (see section F in the supplementary information). The measurements in ambient air and vacuum confirm the previous findings, with a large positive V_{DIRAC} under ambient air and smaller V_{DIRAC} values under vacuum (with similar values of approximately 0.7 V for the different L_{CH}). The details of these measurements are reported in the section E of the supporting information. The complete set of experimental results is summarized in Tab. 1.

4. CONCLUSIONS

The effects of measurement conditions on the extraction of contact related parameters in G-M junctions were investigated in detail using back-gated TLM structures for different metals.

Measurements carried out in ambient conditions, irrespective of the used contact metal, resulted in highly asymmetric transfer curves with positive V_{DIRAC} values, indicating strong p-doping of the graphene channel. Also, a V_{DIRAC} shift in devices with different L_{CH} was observed which is explained on the basis of polycrystalline nature of CVD graphene with non-uniform grain boundaries density.

Vacuum measurements, in contrast, yielded highly symmetric transfer curves for each used metal, which can be reliably used to extract the G-M junction parameters, eliminating one of the main reasons for the scattered values of R_{CF} (and ρ_c) reported in the literature.

Discrepancies related to the extraction of R_{CF} (and ρ_c) via the TLM method were also discussed rigorously. In particular, to extract dependable R_{CF} values, the n_0 in the graphene between the contacts should be kept constant for the different devices (L_{CH}), and hence small differences in V_{DIRAC} position should be compensated. R_{CF} is strongly dependent on the n_0 in the graphene underneath the metal, with the lowest value achieved for gold contacts. The present study highlights the importance of a careful extraction of the contact related parameter in G-M junctions.

Acknowledgements

Financial support from the European Commission (Graphene Flagship, 785219, 881603), the German Ministry for Education and Research, BMBF (GIMMIK, 03XP0210F) and the Italian Minister of Education, University and Research, MIUR (Five2D, 2017SRYEJH) is gratefully acknowledged.

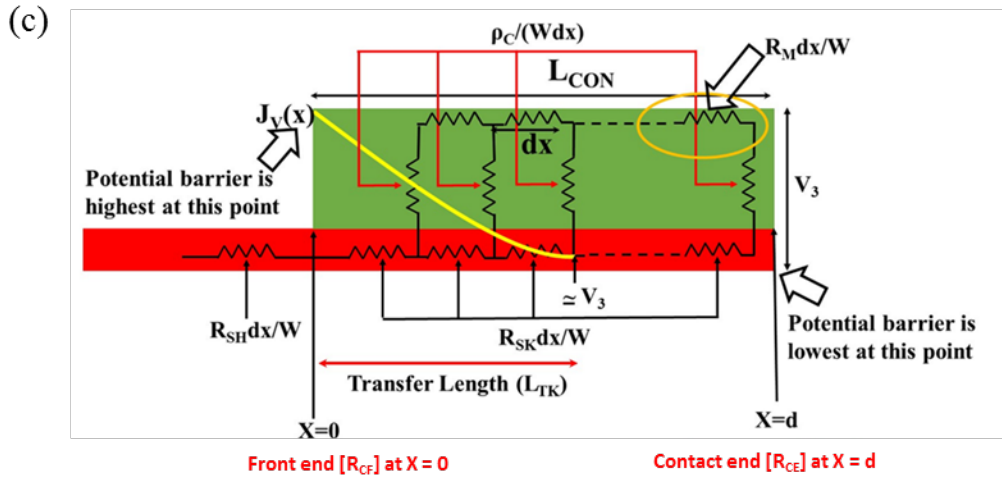
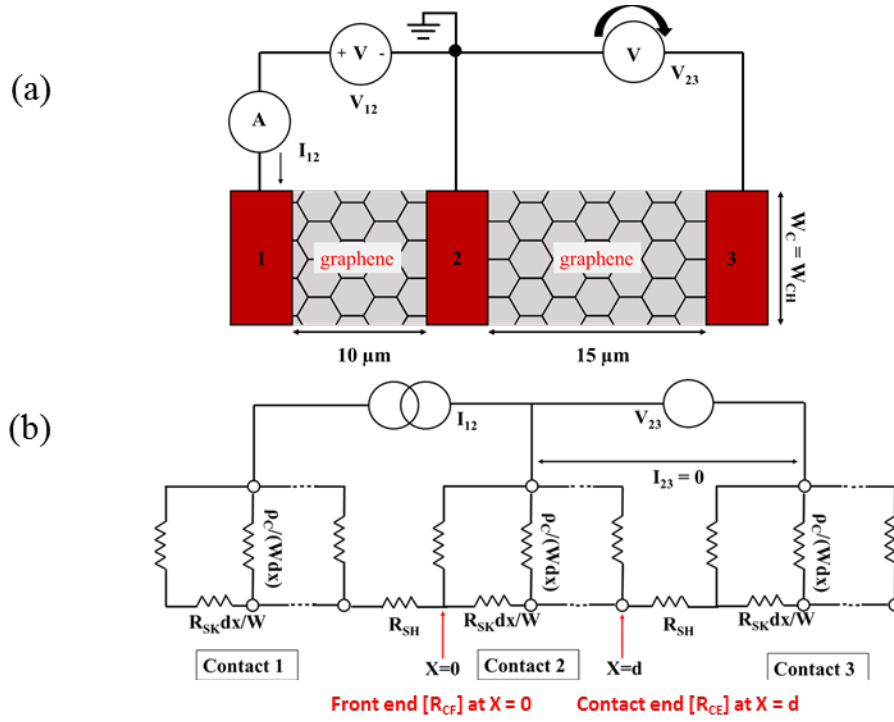
References

- [1] K. S. Novoselov *et al.*, “Electric field effect in atomically thin carbon films,” *Science*, vol. 306, no. 5696, pp. 666–669, 2004.
- [2] Y.-M. Lin, K. A. Jenkins, A. Valdes-Garcia, J. P. Small, D. B. Farmer, and P. Avouris, “Operation of graphene transistors at gigahertz frequencies,” *Nano Lett.*, vol. 9, no. 1, pp. 422–426, 2008.
- [3] Y.-M. Lin *et al.*, “100-GHz transistors from wafer-scale epitaxial graphene,” *Science*, vol. 327, no. 5966, pp. 662–662, 2010.
- [4] L. Liao *et al.*, “High-speed graphene transistors with a self-aligned nanowire gate,” *Nature*, vol. 467, no. 7313, pp. 305–308, 2010.
- [5] G. Fiori and G. Iannaccone, “Insights on radio frequency bilayer graphene FETs,” in *Electron Devices Meeting (IEDM), 2012 IEEE International*, 2012, pp. 17–3, Accessed: Sep. 17, 2017. [Online]. Available: <http://ieeexplore.ieee.org/abstract/document/6479059/>.
- [6] H. Pandey, S. Kataria, A. Gahoi, and M. C. Lemme, “High Voltage Gain Inverters From Artificially Stacked Bilayer CVD Graphene FETs,” *IEEE Electron Device Lett.*, vol. 38, no. 12, pp. 1747–1750, 2017.
- [7] S. Vaziri *et al.*, “Going ballistic: Graphene hot electron transistors,” *Solid State Commun.*, vol. 224, pp. 64–75, 2015.
- [8] T. Mueller, F. Xia, and P. Avouris, “Graphene photodetectors for high-speed optical communications,” *Nat Photon*, vol. 4, pp. 297–301, 2010.
- [9] M. C. Lemme *et al.*, “Gate-Activated Photoresponse in a Graphene p–n Junction,” *Nano Lett.*, vol. 11, no. 10, pp. 4134–4137, Oct. 2011, doi: 10.1021/nl2019068.
- [10] F. Bonaccorso, Z. Sun, T. Hasan, and A. C. Ferrari, “Graphene photonics and optoelectronics,” *Nat. Photonics*, vol. 4, no. 9, pp. 611–622, 2010.
- [11] M. Furchi *et al.*, “Microcavity-integrated graphene photodetector,” *Nano Lett.*, vol. 12, no. 6, pp. 2773–2777, 2012.
- [12] S. Riazimehr *et al.*, “High Responsivity and Quantum Efficiency of Graphene/Silicon Photodiodes Achieved by Interdigitating Schottky and Gated Regions,” *ACS Photonics*, vol. 6, no. 1, pp. 107–115, Jan. 2019, doi: 10.1021/acsp Photonics.8b00951.
- [13] A. D. Smith *et al.*, “Electromechanical piezoresistive sensing in suspended graphene

- membranes,” *Nano Lett.*, vol. 13, no. 7, pp. 3237–3242, 2013.
- [14] C. Chen and J. Hone, “Graphene nanoelectromechanical systems,” *Proc. IEEE*, vol. 101, no. 7, pp. 1766–1779, 2013.
- [15] A. D. Smith *et al.*, “Resistive graphene humidity sensors with rapid and direct electrical readout,” *Nanoscale*, vol. 7, no. 45, pp. 19099–19109, 2015.
- [16] A. D. Smith *et al.*, “Piezoresistive Properties of Suspended Graphene Membranes under Uniaxial and Biaxial Strain in Nanoelectromechanical Pressure Sensors,” *ACS Nano*, vol. 10, no. 11, pp. 9879–9886, Nov. 2016, doi: 10.1021/acsnano.6b02533.
- [17] X. Fan *et al.*, “Graphene ribbons with suspended masses as transducers in ultra-small nanoelectromechanical accelerometers,” *Nat. Electron.*, vol. 2, pp. 394–404, Sep. 2019, doi: 10.1038/s41928-019-0287-1.
- [18] O. Graydon, “Graphene: Terahertz modulator,” *Nat. Photonics*, vol. 9, no. 12, pp. 780–780, 2015.
- [19] B. Sensale-Rodriguez *et al.*, “Broadband graphene terahertz modulators enabled by intraband transitions,” *Nat. Commun.*, vol. 3, p. 780, 2012.
- [20] Q.-Y. Wen *et al.*, “Graphene based all-optical spatial terahertz modulator,” *Sci. Rep.*, vol. 4, 2014.
- [21] D. Neumaier, S. Pindl, and M. C. Lemme, “Integrating graphene into semiconductor fabrication lines,” *Nat. Mater.*, vol. 18, no. 6, p. 525, Jun. 2019, doi: 10.1038/s41563-019-0359-7.
- [22] K. Nagashio and A. Toriumi, “Density-of-states limited contact resistance in graphene field-effect transistors,” *Jpn. J. Appl. Phys.*, vol. 50, no. 7, p. 0108, 2011.
- [23] K. Nagashio, T. Nishimura, K. Kita, and A. Toriumi, “Metal/graphene contact as a performance killer of ultra-high mobility graphene analysis of intrinsic mobility and contact resistance,” in *Electron Devices Meeting (IEDM), 2009 IEEE International*, 2009, pp. 1–4, Accessed: Dec. 30, 2013. [Online]. Available: http://ieeexplore.ieee.org/xpls/abs_all.jsp?arnumber=5424297.
- [24] J. T. Smith, A. D. Franklin, D. B. Farmer, and C. D. Dimitrakopoulos, “Reducing Contact Resistance in Graphene Devices through Contact Area Patterning,” *ACS Nano*, vol. 7, no. 4, pp. 3661–3667, Apr. 2013, doi: 10.1021/nn400671z.
- [25] L. Anzi *et al.*, “Ultra-low contact resistance in graphene devices at the Dirac point,” *2D Mater.*, vol. 5, no. 2, p. 025014, 2018, doi: 10.1088/2053-1583/aaab96.
- [26] V. Passi *et al.*, “Ultralow Specific Contact Resistivity in Metal–Graphene Junctions via Contact Engineering,” *Adv. Mater. Interfaces*, vol. 6, no. 1, p. 1801285, 2019, doi: 10.1002/admi.201801285.
- [27] F. Xia, V. Perebeinos, Y. Lin, Y. Wu, and P. Avouris, “The origins and limits of metal-graphene junction resistance,” *Nat. Nanotechnol.*, vol. 6, no. 3, pp. 179–184, 2011.
- [28] J. S. Moon *et al.*, “Ultra-low resistance ohmic contacts in graphene field effect transistors,” *Appl. Phys. Lett.*, vol. 100, no. 20, pp. 203512–203512, 2012.
- [29] A. Gahoi, S. Wagner, A. Bablich, S. Kataria, V. Passi, and M. C. Lemme, “Contact resistance study of various metal electrodes with CVD graphene,” *Solid-State Electron.*, vol. 125, pp. 234–239, 2016.

- [30] A. Meersha *et al.*, “Record low metal—(CVD) graphene contact resistance using atomic orbital overlap engineering,” in *Electron Devices Meeting (IEDM), 2016 IEEE International*, 2016, pp. 5–3, Accessed: Sep. 08, 2017. [Online]. Available: <http://ieeexplore.ieee.org/abstract/document/7838352/>.
- [31] S. Wang *et al.*, “A more reliable measurement method for metal/graphene contact resistance,” *Nanotechnology*, vol. 26, no. 40, p. 405706, 2015.
- [32] S. Wang *et al.*, “Characterization of the quality of metal–graphene contact with contact end resistance measurement,” *Appl. Phys. A*, vol. 122, no. 7, pp. 1–7, 2016.
- [33] S. Venica, F. Driussi, A. Gahoi, P. Palestri, M. C. Lemme, and L. Selmi, “On the Adequacy of the Transmission Line Model to Describe the Graphene–Metal Contact Resistance,” *IEEE Trans. Electron Devices*, vol. 65, no. 4, pp. 1589–1596, 2018.
- [34] M. König *et al.*, “Accurate graphene-metal junction characterization,” *IEEE J. Electron Devices Soc.*, vol. 7, pp. 219–226, 2019.
- [35] F. Urban, G. Lupina, A. Grillo, N. Martucciello, and A. Di Bartolomeo, “Contact resistance and mobility in back-gate graphene transistors,” *Nano Express*, vol. 1, no. 1, p. 010001, 2020.
- [36] F. Driussi *et al.*, “Improved understanding of metal–graphene contacts,” *Microelectron. Eng.*, p. 111035, 2019.
- [37] A. Di Bartolomeo *et al.*, “Charge transfer and partial pinning at the contacts as the origin of a double dip in the transfer characteristics of graphene-based field-effect transistors,” *Nanotechnology*, vol. 22, no. 27, p. 275702, 2011.
- [38] G. K. Reeves and H. B. Harrison, “Obtaining the specific contact resistance from transmission line model measurements,” *IEEE Electron Device Lett.*, vol. 3, no. 5, pp. 111–113, 1982.
- [39] G. Giovannetti, P. A. Khomyakov, G. Brocks, V. M. Karpan, J. Van den Brink, and P. J. Kelly, “Doping graphene with metal contacts,” *Phys. Rev. Lett.*, vol. 101, no. 2, p. 026803, 2008.
- [40] S. Kataria *et al.*, “Chemical vapor deposited graphene: From synthesis to applications,” *Phys. Status Solidi A*, vol. 211, no. 11, pp. 2439–2449, 2014.
- [41] Y. Wang *et al.*, “Electrochemical delamination of CVD-grown graphene film: toward the recyclable use of copper catalyst,” *ACS Nano*, vol. 5, no. 12, pp. 9927–9933, 2011.
- [42] W. S. Leong, C. T. Nai, and J. T. Thong, “What Does Annealing Do to Metal–Graphene Contacts?,” *Nano Lett.*, vol. 14, no. 7, pp. 3840–3847, 2014.
- [43] S. Wagner *et al.*, “Noninvasive scanning Raman spectroscopy and tomography for graphene membrane characterization,” *Nano Lett.*, vol. 17, no. 3, pp. 1504–1511, 2017.
- [44] Z. H. Ni *et al.*, “The effect of vacuum annealing on graphene,” *J. Raman Spectrosc. Int. J. Orig. Work Asp. Raman Spectrosc. High. Order Process. Also Brillouin Rayleigh Scatt.*, vol. 41, no. 5, pp. 479–483, 2010.
- [45] J. Hong, M. K. Park, E. J. Lee, D. Lee, D. S. Hwang, and S. Ryu, “Origin of new broad Raman D and G peaks in annealed graphene,” *Sci. Rep.*, vol. 3, p. 2700, 2013.
- [46] L. Anzi *et al.*, “Ultra-low contact resistance in graphene devices at the Dirac point,” *2D Mater.*, vol. 5, no. 2, p. 025014, 2018.

- [47] O. Leenaerts, B. Partoens, and F. M. Peeters, “Water on graphene: Hydrophobicity and dipole moment using density functional theory,” *Phys. Rev. B*, vol. 79, no. 23, p. 235440, 2009.
- [48] S.-J. Han, Y. Sun, A. A. Bol, W. Haensch, and Z. Chen, “Study of channel length scaling in large-scale graphene FETs,” in *2010 Symposium on VLSI Technology*, 2010, pp. 231–232.
- [49] A. W. Cummings *et al.*, “Charge Transport in Polycrystalline Graphene: Challenges and Opportunities,” *Adv. Mater.*, vol. 26, no. 30, pp. 5079–5094, 2014, doi: 10.1002/adma.201401389.
- [50] X. Fan *et al.*, “Direct observation of grain boundaries in graphene through vapor hydrofluoric acid (VHF) exposure,” *Sci. Adv.*, vol. 4, no. 5, p. eaar5170, 2018.
- [51] A. Di Bartolomeo *et al.*, “Graphene field effect transistors with niobium contacts and asymmetric transfer characteristics,” *Nanotechnology*, vol. 26, no. 47, p. 475202, 2015.
- [52] A. A. Sagade *et al.*, “Highly air stable passivation of graphene based field effect devices,” *Nanoscale*, vol. 7, no. 8, pp. 3558–3564, 2015, doi: 10.1039/C4NR07457B.
- [53] S. Venica *et al.*, “Reliability analysis of the metal-graphene contact resistance extracted by the transfer length method,” in *2018 IEEE International Conference on Microelectronic Test Structures (ICMTS)*, 2018, pp. 57–62.
- [54] S. S. Cohen and G. S. Gildenblat, *Metal–Semiconductor Contacts and Devices*, vol. 13. Academic Press, 2014.
- [55] A. Dahal and M. Batzill, “Graphene–nickel interfaces: a review,” *Nanoscale*, vol. 6, no. 5, pp. 2548–2562, 2014.
- [56] P. Khakbaz *et al.*, “DFT study of graphene doping due to metal contacts,” in *2019 International Conference on Simulation of Semiconductor Processes and Devices (SISPAD)*, Sep. 2019, pp. 1–4, doi: 10.1109/SISPAD.2019.8870456.
- [57] T. Cusati *et al.*, “Electrical properties of graphene-metal contacts,” *Sci. Rep.*, vol. 7, 2017, Accessed: Sep. 17, 2017. [Online]. Available: <https://www.ncbi.nlm.nih.gov/pmc/articles/PMC5506027/>.
- [58] S. Wittmann *et al.*, “Dielectric surface charge engineering for electrostatic doping of graphene,” *Revis. ACS Appl. Electron. Mater.*, 2020.



(d) Important Notation

R_T (Ω) - total resistance	R_{SK} (Ω/\square) - sheet resistance of the graphene under metal contact
d (μm) - contact length	ρ_c (Ωcm^2) - specific contact resistivity
R_C ($\Omega\mu\text{m}$) - contact resistance	R_{CE} (Ω) - contact end resistance
L_{TK} (μm) - transfer length	R_{SH} (Ω/\square) - sheet resistance of the graphene between the contacts
W_{CH} (μm) - channel width	R_{CF} ($\Omega\mu\text{m}$) - contact front resistance
L_{CH} (μm) - channel length	

Figure 1. (a) Measurement setup for TLM structures. (b) Equivalent circuit diagram describing the distributed resistive components in a TLM structure. (c) Distributed circuit diagram of the transmission line model to describe the G-M contact. $X=0$ is front of the contact and $X=d$ is end of the contact (d = length of the contact). The horizontal voltage drop due to the graphene resistance leads to the current crowding at the G-M junction. (d) Important notation used in this paper.

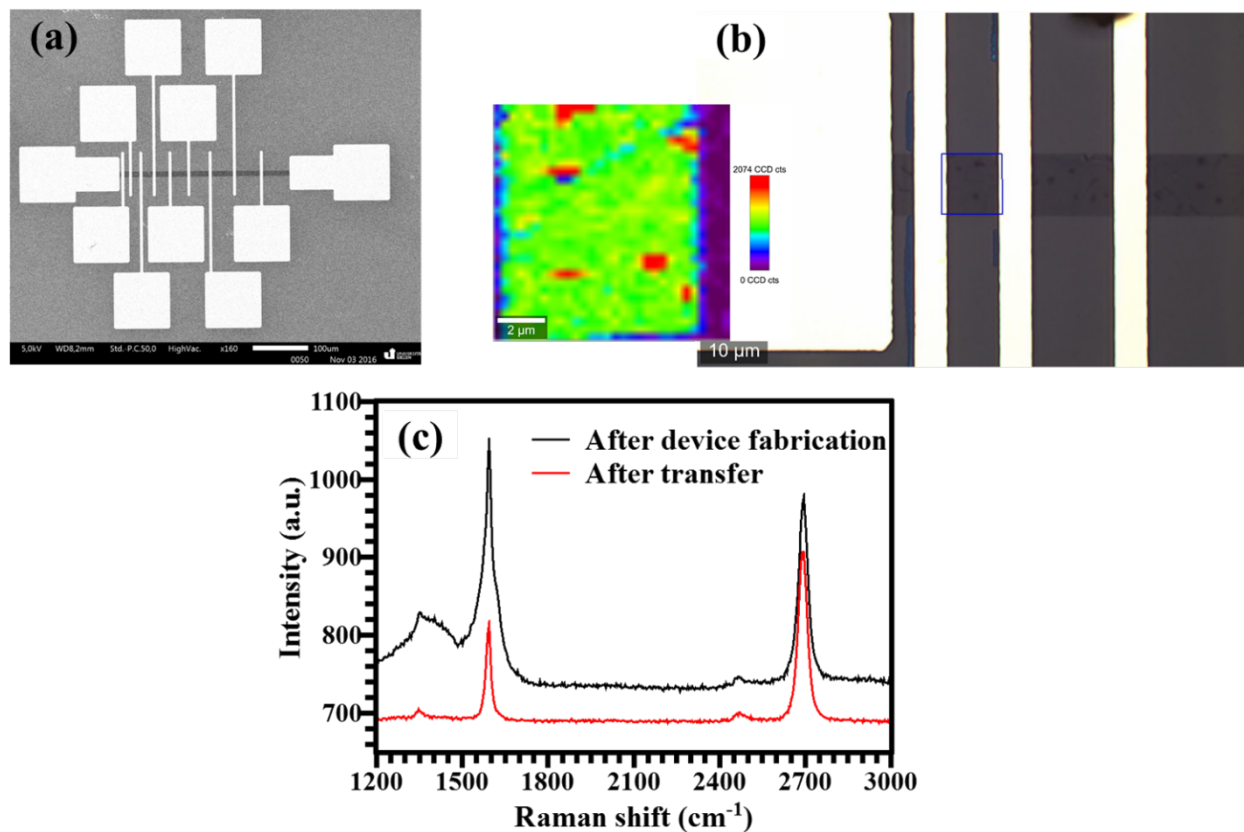


Figure 2. (a) Scanning electron micrograph (SEM) of a graphene FET array (TLM structures. (b) Raman area map of 2D peak in the area depicted by the blue square in the optical micrograph of the device. (c) Raman spectrum of a CVD graphene transferred on a SiO₂/Si substrate.

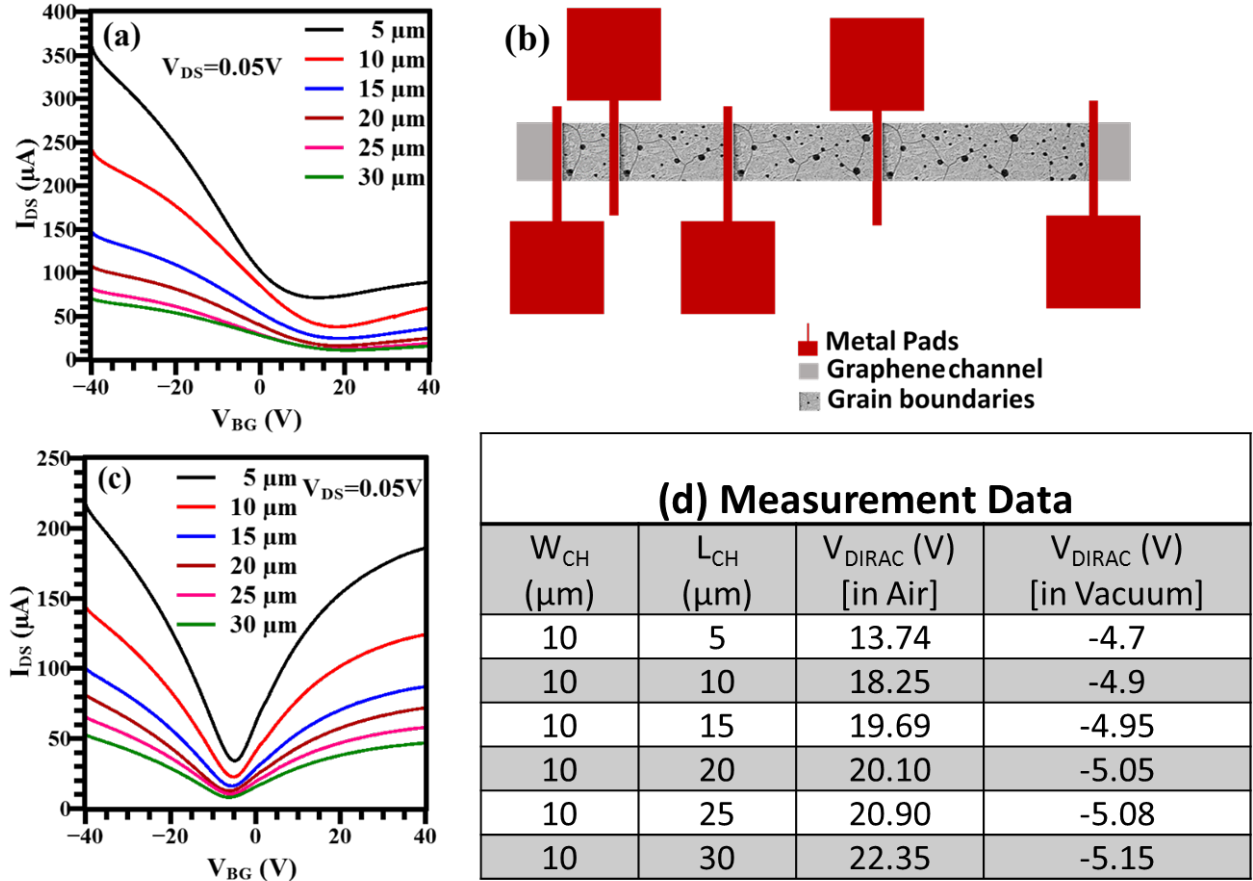


Figure 3. (a) Transfer characteristics (I_{DS} vs V_{BG}) measured in ambient atmosphere (humidity ~21%, temperature ~300K). (b) Schematic structure of a TLM structure depicting grain boundaries or line defects in the CVD graphene. (c) Transfer characteristics (I_{DS} vs V_{BG}) measured in high vacuum (humidity ~0%, temperature ~300 K, Pressure ~ 10^{-7} mbar). (d) Summary of a data in a tabular form focusing on V_{DIRAC} position measured in ambient air and in vacuum.

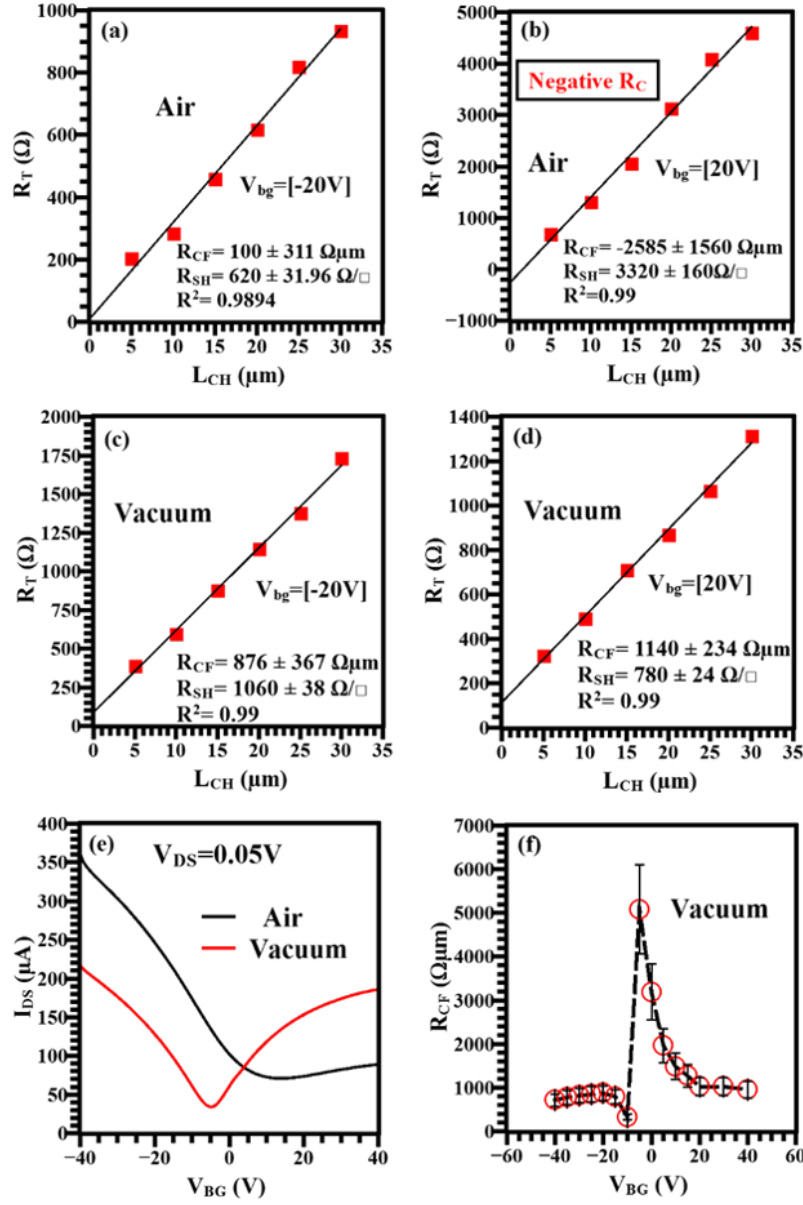


Figure 4. Extrapolation of R_{CF} and R_{SH} by using the transfer characteristics curves of graphene - nickel samples [Fig. 3(a)] measured in ambient atmosphere at gate biases of -20 V (a, p-doped) and 20 V (b, n-doped). Red squares represent measured total resistance; black line, is the linear fitting curve. R_{CF} and R_{SH} are also extrapolated by using the transfer characteristics curves [Fig. 3 (c)] measured in high vacuum at gate biases of -20 V (c) and 20 V (d). (e) Comparison of transfer characteristics measured in air and vacuum. (f) R_{CF} as a function of a V_{BG} .

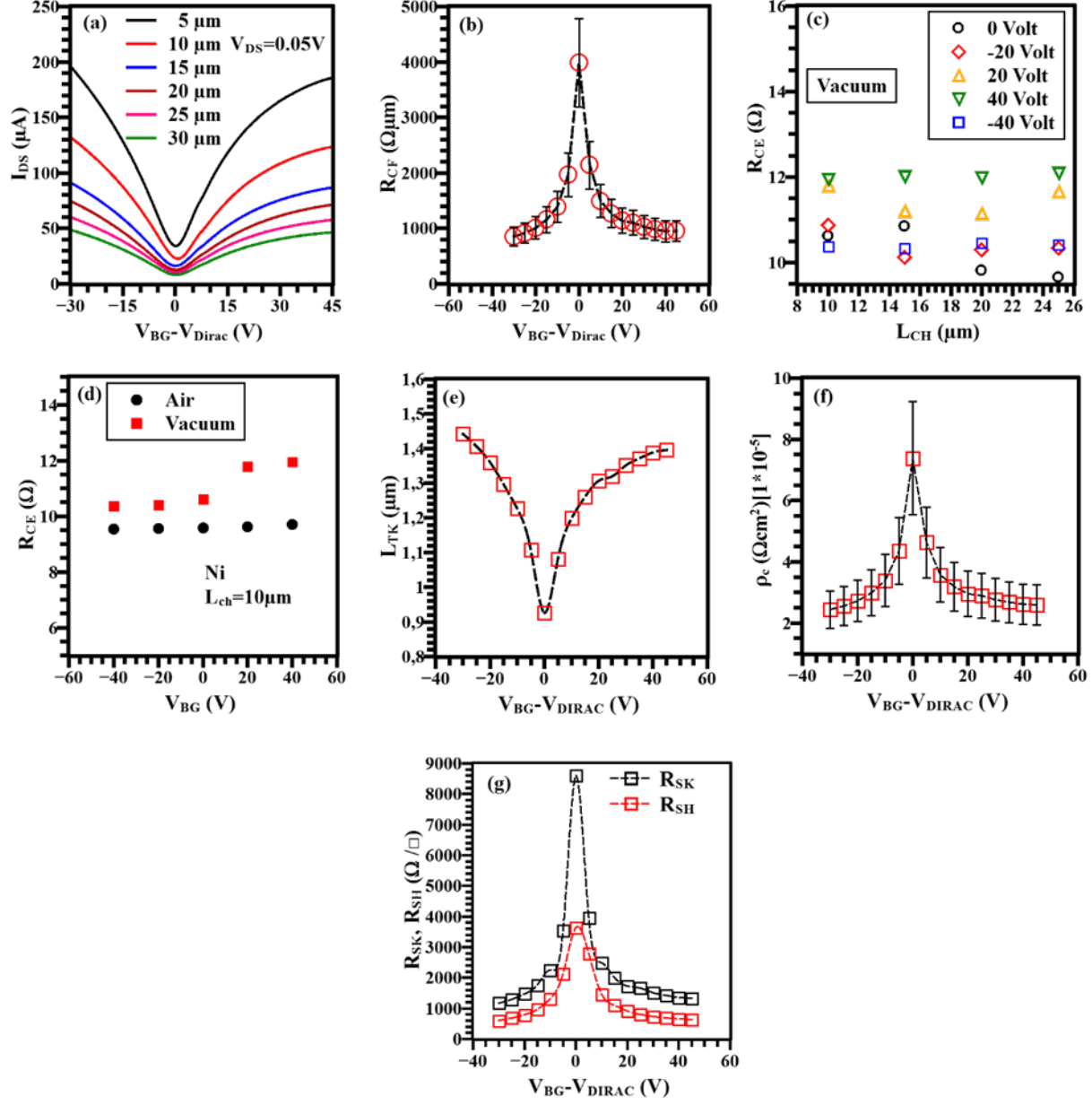


Figure 5. (a) Transfer characteristics of G-Ni TLM structures after normalizing to $V_{Dirac} = 0$ V the curves of Fig. 3 (c). (b) R_{CF} as a function of $V_{BG} - V_{Dirac}$. (c) R_{CE} as a function of L_{CH} measured at different V_{BG} . (d) R_{CE} as a function of V_{BG} in ambient atmosphere and in vacuum. (e) L_{TK} and (f) ρ_c as a function of $V_{BG} - V_{Dirac}$. (g) R_{SK} and R_{SH} as a function of $V_{BG} - V_{Dirac}$.

Table 1: - Summary of results

Graphene – Metal Contact	(R_{CF}) ($\Omega\mu\text{m}$)	L_{TK}) (μm)	R_{SK} (Ω/\square)	R_{SH} (Ω/\square)	ρ_c (Ωcm^2)
G-Ni (n = $8.69 \times 10^{12} \text{ cm}^{-2}$)	853 \pm 171	1.45	1174	608	2.44×10^{-5}
G-Cu (n = $1.15 \times 10^{13} \text{ cm}^{-2}$)	860 \pm 172	1.63	417	729	1.1×10^{-5}
G-Au (n = $1.07 \times 10^{13} \text{ cm}^{-2}$)	395 \pm 79	1.68	376	425	7.16×10^{-6}
G-Ni (n = $1.01 \times 10^{12} \text{ cm}^{-2}$)	3984 \pm 799	0.93	8599	3642	7.38×10^{-5}
G-Cu (n = $1.34 \times 10^{12} \text{ cm}^{-2}$)	3664 \pm 733	0.97	3359	3540	3.5×10^{-5}
G-Au (n = $1.06 \times 10^{12} \text{ cm}^{-2}$)	1303 \pm 261	0.97	1081	2700	1.56×10^{-5}